Numerical modeling of a moderate hydrogen leakage in a typical two-vented fuel cell configuration

E Saikali[†,*], P Ledac[†], A Bruneton[†], A Khizar[†], C Bourcier[†], G Bernard-Michel[†], E Adam[†] and D Houssin-Agbomson[‡]

[†] *Université Paris-Saclay, CEA,*
Service de Thermo-hydraulique et de Mécanique des Fluides,
91191, Gif-sur-Yvette, France,
[‡] *Air Liquide, Research & Development - Innovation Campus Paris,*
78354, Les loges-en-Josas, France,
[*] *Corresponding author: elie.saikali@cea.fr*

Abstract

Numerical results are presented from two direct numerical simulations (DNS) where a moderate hydrogen leakage is modeled in a typical two-vented fuel cell configuration. The study mimics one of the experimental investigations carried out on the 1 m^3 enclosure with a leak flow rate of 10.4 $Nl.min^{-1}$ [1]. The injection dimensionless Richardson number is at the order of unity and thus characterizes a plume flow which becomes turbulent due to gravitational accelerations. Two large exterior regions are added to the computational domain to model correctly the exchange between the in/out flows at both vents and the outer environment. Two meshes are used in this study; a first consisting of 250 million cells, while the second has 2 billion cells to ensure the fine DNS resolution at the level of Kolmogorov and Batchelor length scales. The high performance computation (HPC) platform TRUST is employed where the computational domain is distributed up to 5.10^4 central processing unit (CPU) cores. A detailed description of the flow structure and the hydrogen dispersion is provided where the sharp effect of the cross-flow on the plume is analyzed. Comparisons versus the experimental measurements show a very good agreement where both the bi-layer Linden regime and the maximal concentration in the top homogeneous layer are correctly reproduced by the DNS. This result is extremely important and breaks the limitations shown previously with statistical RANS approaches and LES models. This study can be considered as a good candidate for any further improvements of the theoretical industrial plume models in general, and for the estimation of the non-constant entrainment coefficient in particular.

I. CONTEXT

This study is placed in the context of safety assessment of systems using hydrogen as an energy carrier. In such applications, hydrogen is stored inside cylinders under compressed form (pressure can reach up to 700 bar), and is distributed afterwards by the means of pipes to supply the system and to produce energy. In a typical accidental scenario originating from a human or a technical error, hydrogen escapes in the confinement and entrains air from all directions to form a highly dangerous and flammable mixture with hazardous consequences; the critical hydrogen volume fraction in air is between $4 - 75\%$ [2]. Ventilated cavities with simplified passive ventilation designs are usually considered to reduce the hydrogen accumulation that can build in such accidental scenarios and therefore can help to avoid severe problems [3].

Since the applications of the indoor-use hydrogen systems are widely spreading nowadays, a good

DNS	Direct numerical simulations		$< \cdot >_t$	Time averaging operator	
am	Subscript denoting ambient		in	Subscript denoting injection	
Ri	Richardson number	[-]	Re	Reynolds number	[-]
Ma	Mach number	[-]	$\mathcal{O}$	Cartesian system's origin	[-]
Y_1	Hydrogen mass fraction	[-]	X_1	Hydrogen volume fraction	[-]
t	Time	[s]	δt	Time step	[s]
δ	Mesh step size	[m]	$\mathbf{x}$	Space vector	[m]
η	Kolmogorov length scale	[m]	W	Horizontal width of cavity	[m]
L	Span-wise length of cavity	[m]	H	Height of cavity	[m]
d	Diameter of pipe	[m]	h	Height of pipe	[m]
p	Thermodynamic pressure	[Pa]	P	Hydrodynamic pressure	[Pa]
τ	Viscous stress tensor	[Pa]	T	Temperature	[K]
$\mathbf{u}$	Mixture mass velocity vector	[m.s^{-1}]	g	Gravity vector	[m.s^{-2}]
D	Mixture diffusion coefficient	[m^2.s^{-1}]	ρ	Density	[Kg.m^{-3}]
M	Molar mass	[Kg.mol^{-1}]	μ	Dynamic viscosity	[Kg.m^{-1}.s^{-1}]
R	Specific gas constant	[J.K^{-1}.mol^{-1}]			

Nomenclature

understanding of the risk that can be induced by such a green vector of energy is necessary. In order to correctly provide consequence assessments and safety recommendations that concern this problematic, a well validated scientific research is required to predict correctly the behavior and the build-up of the hydrogen/air mixture in such severe accidents. The predictions should quantify the effect of the passive ventilation in reducing the hydrogen accumulation, in addition to the maximal concentration in the homogeneous layer that usually develops in such configurations [4].

Three approaches are usually employed in such studies; theoretical models, experimental measurements and/or numerical simulations. This paper is based on a numerical computational fluid dynamics (CFD) approach where a moderate hydrogen leakage is analyzed from direct numerical simulations (DNS). The two-vents experimental cavity DRHyS (1 m^3) is studied, where it reproduces a classical two vented fuel cell configuration with an enhanced passive ventilation system [1].

Two numerical benchmarks had been carried out on the same experimental configuration with a wide range of injection Richardson number (Ri) varying from 10^{-1} to 10^2 [5, 6]. Numerical results had shown that statistically-averaged RANS and spatially-averaged LES approaches introduce limitations when the hydrogen leakage is characterized by a buoyant-jet flow regime; typically for Ri close to unity. In such a particular flow regime, the results had shown that RANS models are too diffusive and highly overestimate the hydrogen concentration in the cavity, whereas the LES do not predict a correct bi-layer regime reported in the experiments [5, 6]. Much better results had been reported when the flow regime is described as a pure jet flow; typically for Ri < 1.

The necessity of performing DNS for buoyant-jet flows has been highlighted in a recent work carried out by [7, 8] on a two vented cavity with a reduced volume (3.7×10^{-4} m^3). In their study, the concerned authors presented detailed validation and showed that the LES Smagorinsky model highly underestimates the fluctuations in the release vicinity, and therefore can not predict correctly

the plume structure in the upper part of the cavity. By comparing to particle image velocimetry (PIV) measurements, the same authors showed in [9] that a well resolved DNS satisfactory predicts the plume structure and thus conclude that such results can serve for safety recommendations.

This study aims at providing reference DNS data for a buoyant-jet flow regime with Ri $\approx 10^1$. It is extremely important to emphasize that a DNS for such a volume has never been carried out and is not reported in the literature. A complete description and analysis of the 3D instantaneous/statistical fields is presented. For this reason, the provided numerical data can serve as a base reference for future comparisons and benchmarks. A brief outline of the paper follows. The physical model and the numerical methods are discussed in section two. Section three describes the computational setup and some high performance computing (HPC) details. Numerical results and reference data are presented in section four. Conclusions and future perspectives are drawn finally in section five.

II. MODELING

A. Physical and numerical configurations

As stated previously, the numerical study mimics the experimental work carried out on the DRHyS experimental cavity. Pure hydrogen gas is injected through a cylindrical pipe into a two vented parallelepiped enclosure filled initially with air at rest. A continuous/constant volumetric flow-rate $Q = 10.4$ Nl.min$^{-1} \approx 1.8 \times 10^{-4}$m^3.s^{-1} is considered. Otherwise stated, the lower script "*in*" will refer to the injected hydrogen, while the "*am*" lower script is used to denote the ambient air.

The considered enclosure has a cuboid shape with a volume capacity of 1 m^3; square base of $W = L = 0.995$ m and height $H = 1$ m. A cylindrical injection pipe of diameter $d = 2.72 \times 10^{-2}$ m is considered. The release point is centered in the horizontal section of the enclosure and located at an altitude of 0.08 m. Two vents located on two opposite vertical walls are considered to enhance the passive ventilation, respectively at the top and at the bottom. Both openings have an identical surface area equals to 0.18×0.96 m^2 (see figure 1). Plexi-glass of thickness 5×10^{-3} m is used for the solid wall boundaries.

To measure the hydrogen volume fraction in the enclosure, 15 minicatharometers Xen-TCG3880 from Xensor Integration have been used in the experimental study. As shown in figure 1, these sensors are located all along the height H near the left wall with an equidistant inter-distance equals to 0.065 m. The absolute accuracy of the minicatharometers was assessed to be around 0.1% vol of hydrogen. The sensors can measure the concentration fluctuations down to 0.05%. The reactivity of those sensors is assessed to be around 1 s. Additional information regarding the experimental setup and the measuring accuracy can be reviewed from [1].

The temperature T and the thermodynamic pressure p had been verified to be constant and not varying during the experimental study; $T = 11°$ C and $p = 1$ atm. Under these conditions, the physical properties of the working fluids is summarized in table I.

Characteristics of the flow regime are given in terms of the dimensionless injection Richardson and

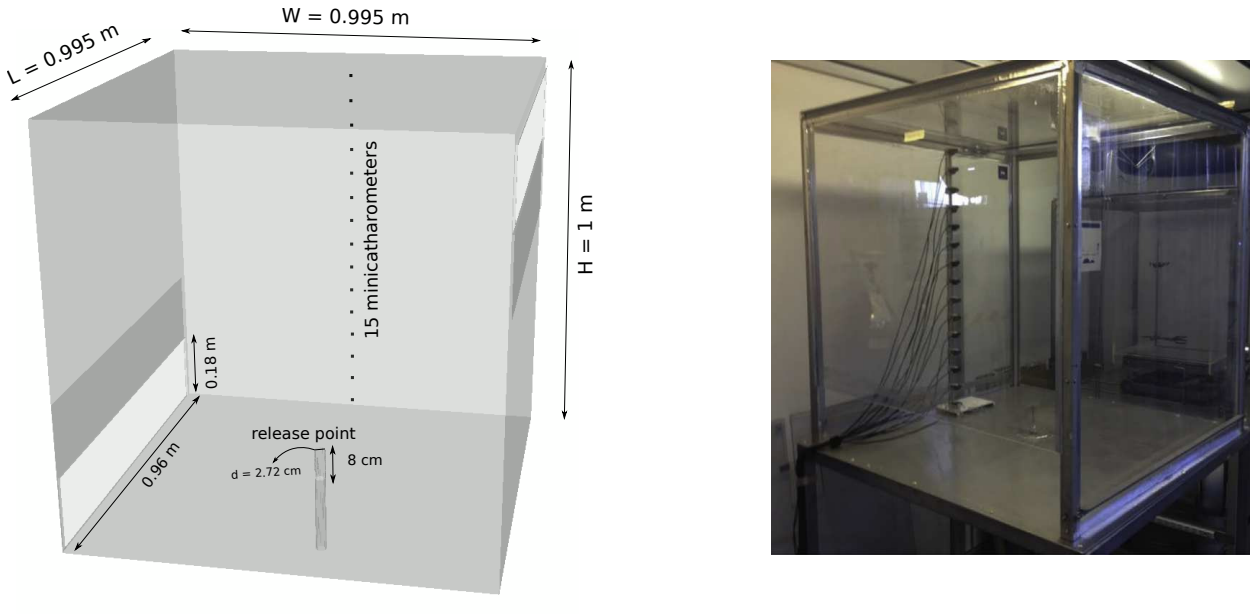

FIG. 1: Two-vents 1 m^3 facility. Left: schematic representation, right: real configuration.

Fluid	**Density** [kg.m^{-3}]	**Dynamic viscosity** [$\times 10^{-5}$ kg.m^{-1}.s^{-1}]	**Molar mass** [$\times 10^{-2}$kg.mol^{-1}]
Injected Hydrogen	$\rho_{in} = 0.08533$	$\mu_{in} = 0.86269$	$M_{in} = 0.20159$
Ambient Air	$\rho_{am} = 1.226$	$\mu_{am} = 1.792$	$M_{am} = 2.897$

TABLE I: Physical properties of the working fluids at $T = 11°$ C and $p = 1$ atm.

Reynolds numbers at the injection

$$\mathrm{Ri}_{in} = \frac{g(\rho_{am} - \rho_{in})\ d}{\rho_{in} u_{in}^2} \approx 10 \quad \text{and} \quad \mathrm{Re}_{in} = \frac{\rho_{in} u_{in}\ d}{\mu_{in}} \approx 162,$$

where u_{in} is the maximum injection velocity equals to 0.6 m.s^{-1} (parabolic profile).

In the numerical study, the dimensions of the cavity and the two vents, in addition to the pipe's diameter d are kept the same. However, the height of the pipe h is limited to 0.28 m (0.08 m into the cavity and 0.2 outside). A parabolic velocity profile is considered at the entrance (bottom) of the pipe to make sure that the velocity distribution along the pipe matches the fully developed steady state solution in the real experiment. We have verified by numerical simulations that this height is sufficient and that there is no impact on the solution if a longer tube is modeled.

B. Governing equations

The flow is governed by the conservation equations of mass, momentum and species. The equation of state for a binary gas mixture is used to relate the mixture's density with the species mass

fractions [10]. The energy conservation equation is not required here as far as the iso-thermal and iso-bar conditions are valid. Owing to the smallness of the Mach number, together with the large ambient-to-injection density ratio $\rho_{am}/\rho_{in} \approx 14$, a low Mach number (LMN) approximation of the conservation equations is appropriate. In this approximation, and following an asymptotic analysis, the total pressure splits as the sum of a spatially uniform and constant thermodynamic pressure $p(t)$ and a hydrodynamic pressure $P(\mathbf{x}, t)$ dependent on both space and time [11, 12] (here $\mathbf{x}$ denotes the space coordinate vector).

The dimensional system of governing equations under the LMN approximation thus reads

$$\frac{\partial \rho}{\partial t} + \frac{\partial}{\partial x_i}\Big(\rho u_i\Big) = 0, \tag{1}$$

$$\frac{\partial \rho u_j}{\partial t} + \frac{\partial}{\partial x_i}\Big(\rho u_j u_i\Big) = -\frac{\partial P}{\partial x_j} + \frac{\partial \tau_{ij}}{\partial x_i} + \rho g_j, \tag{2}$$

$$\frac{\partial \rho Y_1}{\partial t} + \frac{\partial}{\partial x_i}\Big(\rho u_i Y_1\Big) = \frac{\partial}{\partial x_i}\Big(\rho\, D \frac{\partial Y_1}{\partial x_i}\Big), \tag{3}$$

$$\rho = M_{mix}\frac{p}{RT}, \tag{4}$$

where ρ is the mixture's density and u_i the mass average component of the velocity vector $\mathbf{u} = (u_1, u_2, u_3)$ and $g_j = (0, 0, -g)$ the gravity vector. Y_1 and Y_2 are respectively the hydrogen and air mass fractions satisfying $Y_1 + Y_2 = 1$. $D = 7.72 \times 10^{-5}$ m^2.s^{-1} corresponds to the mixture diffusion coefficient, $R = 8.314$ J.K^{-1}.mol^{-1} the specific gas constant and $M_{mix} = \left(\sum_{i=1}^{2} \frac{Y_i}{M_i}\right)^{-1}$ the mixing molar mass where $M_1 = M_{in}$ and $M_2 = M_{am}$, the injection and ambient molar mass respectively (recall table I). $\tau_{ij} = 2\mu e_{ij}$ is the viscous stress tensor for Newtonian fluids with

$$e_{ij} = \frac{1}{2}\left(\frac{\partial u_i}{\partial x_j} + \frac{\partial u_j}{\partial x_i}\right) - \frac{1}{3}\delta_{ij}\frac{\partial u_k}{\partial x_k},$$

and δ_{ij} the Kronecker symbol. μ denotes the mixture's dynamic viscosity calculated as a function of the mass fractions and fluids physical properties using the Wilke's formulation [13] as follows

$$\mu = \frac{Y_1\mu_1}{Y_1\phi_{11} + Y_2\phi_{12}} + \frac{Y_2\mu_2}{Y_1\phi_{21} + Y_2\phi_{22}}, \tag{5}$$

where ϕ_{ij} is a set of dimensionless constants calculated as

$$\phi_{ij} = \frac{\frac{\mathrm{M}_i}{\mathrm{M}_j}\left[1 + \left(\frac{\mu_i}{\mu_j}\right)^{1/2}\left(\frac{\mathrm{M}_j}{\mathrm{M}_i}\right)^{1/4}\right]^2}{\left[8\left(1 + \frac{\mathrm{M}_i}{\mathrm{M}_j}\right)\right]^{1/2}} \quad : \quad i, j = \{1, 2\}. \tag{6}$$

Figure 2 depicts the evolution of the mixture's dynamic viscosity μ (left), of ρ (middle) and the mixture's kinematic viscosity $\nu = \mu/\rho$ [m^2.s^{-1}] (right) as a function of the hydrogen mass fraction Y_1.

It can be clearly noted that the variation of mixture's physical properties is important. For example, the variation of ν near the nozzle where the hydrogen leak takes place can reach 20%, while about 90% upstream in the plume where Y_1 values can be very small.

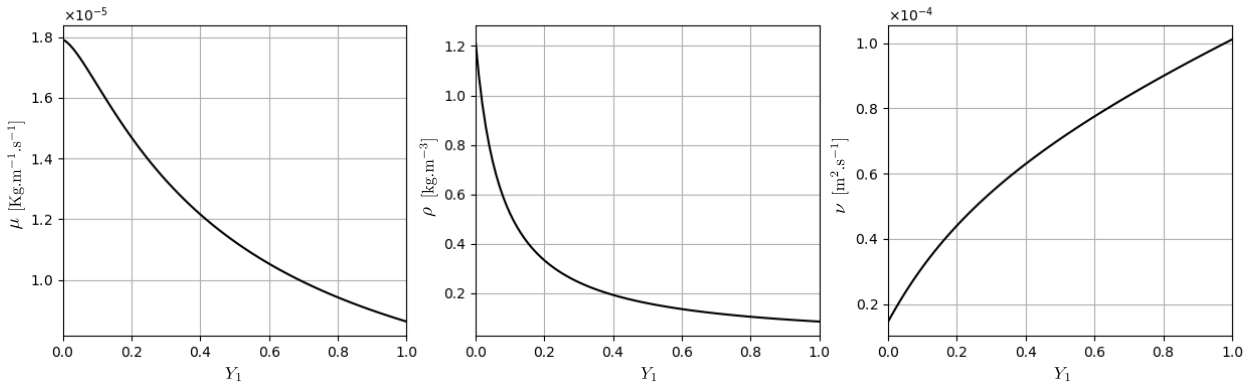

FIG. 2: Variation of the mixture's dynamic viscosity μ (left), ρ (middle) and ν (right) versus the hydrogen mass fraction Y_1 at the considered iso-thermal and iso-bar conditions: $T = 11°$ C and $p = 1$ atm.

In what follows, the hydrogen concentration is mostly expressed in terms of volume fraction X_1. The relationship between the mass and the volume fractions reads as

$$X_1 = (\rho - \rho_{\text{amb}})/(\rho_{\text{inj}} - \rho_{\text{amb}}) = \rho Y_1/\rho_{\text{inj}}. \tag{7}$$

III. NUMERICAL SET-UP

A. CFD software and numerical methods

Numerical simulations are performed by the open source code TRUST (TRio_U Software for Thermohydraulics) developped at the energy division (DES) of the French atomic commission (CEA) [14]. The code is based on an object oriented intrinsically parallel approach, and is written in the C++ language. The METIS library is used to perform HPC simulations where the computational domain is decomposed into several overlapping sub-domains. METIS always insures a small load imbalance of the domain partition (defined by the product of the maximum cells among sub-domains and the number of sub-domains divided by the total number of cells). As a result, all sub-domains are normally distributed quite equally among different processor cores, which, by using message passing interface libraries (MPI), communicate only with required neighbor processors when data transfer is needed. All I/O processes are parallelized with the possibility to read and write from a single file (with the HDF5 library) or from distributed files. When a calculation domain comprises more than $2^{31}/8$ cells (about 268.5 million cells), the integers need to be represented on 64 bits. This feature is included as a compiler option.

The spatial discretization is based on a Finite Difference Volume (FDV) method, which is implemented on a staggered grid of type Marker and Cell (MAC). Spatial derivatives are discretized by a second ordered centered scheme except for the convective term of the species equation (3) where a third order quadratic upstream interpolation for convective kinematics (QUICK) scheme is used to ensure the monotonicity preserving constraints and that $Y_1 \in [0, 1]$.

The system of equations is solved in a sequential way at each time iteration using a semi-implicit

scheme, which treats implicitly the diffusion terms and explicitly the convective ones. Thus, the time step δt is dynamically selected at each iteration satisfying the convective CFL = 1 criterion. Linear systems resulting from the implicit treatment of the diffusion terms are solved by a conjugate gradient method (CGM) [15]. The PETSc library is used in this study [16].

To solve the pressure-velocity coupling, an incremental projection method is employed where the variable of the Poisson equation is the pressure increment $\delta P = P^{t+\delta t} - P^t$. The obtained elliptic Poisson equation which is solved by an iterative symmetric successive over relaxation (SSOR) method. δP is finally used for correcting the velocity field over the domain to satisfy the divergence constraint obtained from equation (1) and expressed as

$$\frac{\partial u_i}{\partial x_i} = -\frac{1}{\rho}\frac{D\rho}{Dt}, \tag{8}$$

where $\frac{D}{Dt} = \frac{\partial}{\partial t} + u_i \cdot \frac{\partial}{\partial x_i}$ denotes the material derivative operator.

B. Computational domains and meshing

To satisfactorily approach the natural inlet/outlet boundary conditions and in order to model correctly the exchange between the in/out flows at both vents and the outer environment, the same approach used in [7] is followed. Two large exterior regions are added to the computational domain near both vents respectively at the left-bottom and top-right of the cavity (see figure 3, red surfaces). As a consequence, the numerical outlet boundary conditions are shifted away from the vents. We denote by L_x, L_y and L_z the horizontal, span-wise and vertical dimensions respectively for each exterior region. Their dimensions, in addition to the total volume of each region, are summarized in table II.

Exterior region	Lx **[m]**	Ly **[m]**	Lz **[m]**	**Volume [m^3]**
Lower	1	1.32	0.54	0.713
Upper	1	1.32	0.72	0.95

TABLE II: Dimensions of the exterior regions added to the computational domain.

Following the work of Chhabra et al. in [17] and considering the injection conditions, the Kolmogorov length scale can be estimated for this problem as $\eta = 8 \times 10^{-4}$ m. Since the mixing/dissipation of the species are significant in this study, the Batchelor length scale λ_B should also be considered [18]. The Batchelor length scale is defined as $\lambda_B = \eta/\sqrt{\mathrm{Sc}}$, with $\mathrm{Sc} = \nu/D$ being the Schmidt number. It can be clearly shown that the turbulent length scales which are dominant in this problem are those at the same order of η. This observation is true as far as λ_B is only significant near the nozzle where the flow is laminar; recall that $\mathrm{Re}_{inj} \approx 162$.

In accordance with the estimations of η and λ_B, two meshes have been used for this study; referred to as Mesh 1 and Mesh 2 respectively. In both cases, a non-uniform unstructured cubic mesh has been generated via the open source SALOME platform, thanks to the Hexahedron (i, j, k) and the body fitting algorithms [19]. The origin of the Cartesian system $\mathcal{O}(0, 0, 0)$ is placed in the middle

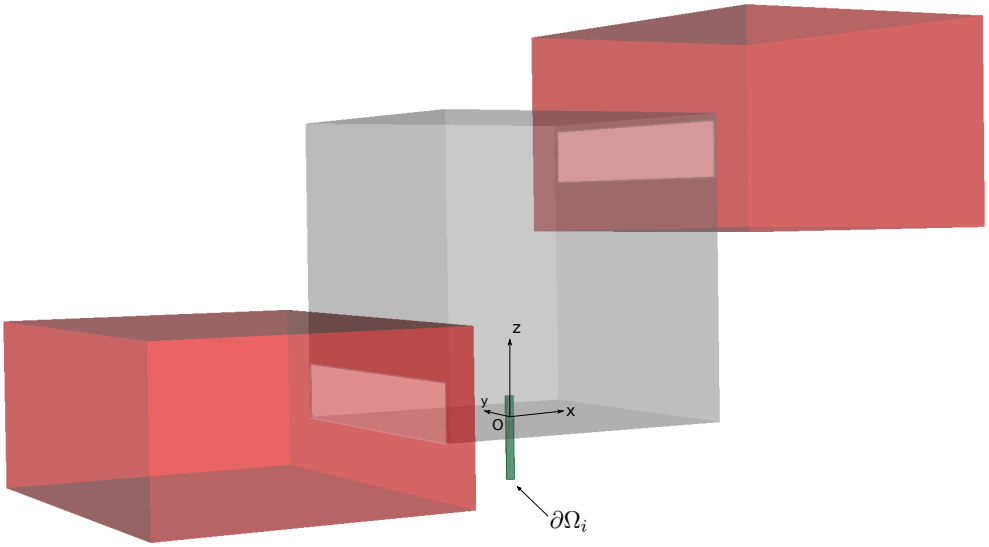

FIG. 3: Schematic representation of the DNS computational domain: exterior regions in red color, solid boundaries (cavity and pipe) in gray and green.

of the cavity at the bottom as shown in figure 3. A layer of 5×10^{-3} m width around the vents is also meshed to take into account the thickness of the plexi-glass in the real experiment. The generated meshes are described as follows:

- Mesh 1:

Mesh 1 consists in total of 250 million cubes distributed over 5376 MPI procs ($\approx$ 47000 cells per proc). The step size δ is non-uniform in the computational domain and varies from 1 mm to 4 cm, taking into account a good quality of the aspect ratio and the evolution of the cell stretching.

Smallest sizes of $\delta = \min\{\delta_x, \delta_y, \delta_z\}$ are located inside the cavity and in the vicinity of the vents. In the injection tube, the smallest $\delta = 1$ mm is used to capture correctly the diffusion phenomenon that takes place. Similarly, a fine resolution is considered at the middle all along the height of the cavity in a circular region of radius 0.25 m to capture correctly the turbulent scales that will develop at the edge of the plume. In the far field, the mesh is coarser where the step size can reach $\delta = 3.5$ mm. This is justified by the fact that the mixing that takes place in the far field is controlled by the convected flow rather than the turbulence; basically by the large scale rotational vortices that build-up at the top of the cavity. Figure 4 depicts the δ/η ratio in the mid-vertical xz-plane at $y = 0$ and thus justifies the employed values of δ.

Outside the cavity (i.e. in the exterior regions), a coarse mesh is used with a systematically stretched grid size varying from $\delta = 4.5$ mm near the vents up to $\delta = 4$ cm very far away from the cavity. Recall that these regions are not in our interest and they are just considered to shift the numerical boundary conditions away from the cavity. Figure 5 depicts a 2D view of Mesh 1 in the mid-vertical xz-plane at $y = 0$ with the variation of δ in the region of interest.

- Mesh 2:

Mesh 2 consists in total of 2 billion cubes distributed over 50047 MPI procs ($\approx$ 40000 cells per

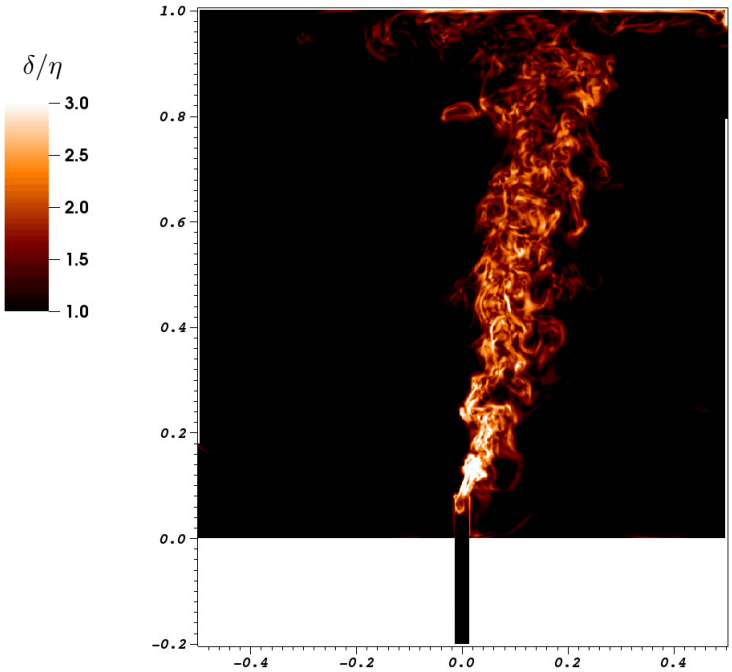

FIG. 4: Mesh 1: iso-contours of the ratio δ/η in the mid-vertical xz-plane at $y = 0$.

proc). It is based on Mesh 1 where each cube is divided into 8 sub-cubes. As a consequence, the same quality as the previous mesh is obtained. However, the step size δ of Mesh 2 varies from 0.5 mm to 2 cm. Being smaller than the predicted Kolmogorov and Batchelor length scales, the results obtained with Mesh 2 will be referred to as the reference DNS solution.

C. Boundary conditions

The boundary conditions are described as follows. At the inlet boundary $\partial\Omega_i$ situated at the bottom end of the pipe, a fixed convective mass flux equal to $\rho_{in}Q$ is imposed with flat profiles for $\rho = \rho_{in}$ and $Y_1 = 1$; recall that $Q = 10.4$ Nl.min^{-1}. On the contrary, a parabolic profile is imposed for $\mathbf{u}$ so that the velocity vector is oriented along the z-direction. Since the mesh is hexahedral, a stair-step like grid is generated by the body-fitting algorithm of SALOME in order to model the cylindrical injection pipe. As a consequence, the prescribed velocity profile is defined as

$$u_3 = \epsilon_Q \times u_3^*,$$

where u_3^* is a predicted parabolic profile defined in terms of the pipe diameter d and the horizontal $x-y$ coordinates as $u_3^* = d^2/4-(x^2+y^2)$. ϵ_Q is a correction parameter used to ensure the volumetric flow-rate conservation and is thus calculated as

$$\epsilon_Q = \frac{Q}{\int\int_{\partial\Omega_i} u_3^* dxdy}.$$

Figure 6 depicts for example the parabolic distribution of the vertical velocity u_3 prescribed at $\partial\Omega_i$ for Mesh 1.

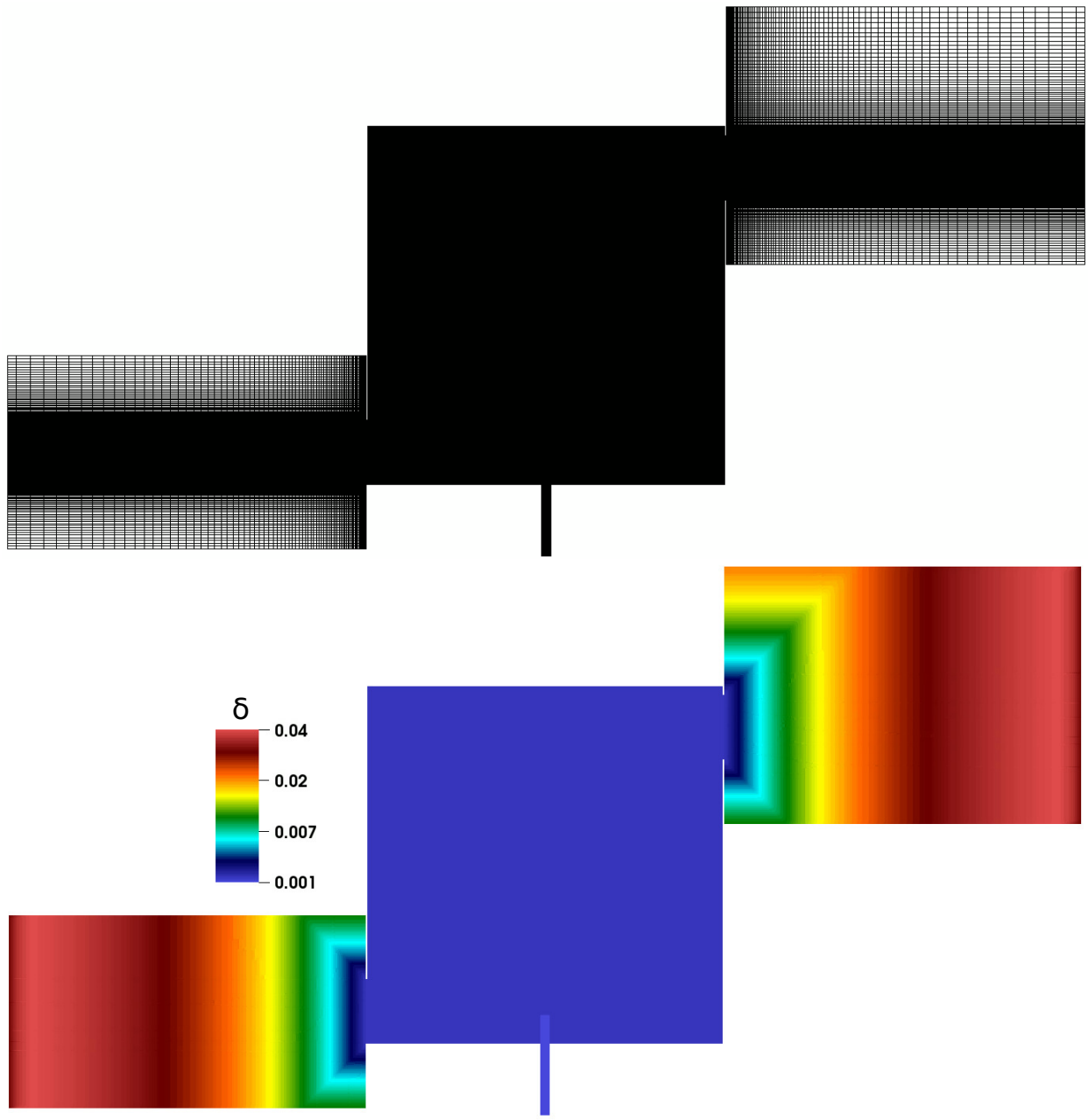

FIG. 5: 2D visualization of Mesh 1 in the mid-vertical xz-plane at $y = 0$. Top: the employed mesh, bottom: the step size δ.

On the wall boundaries (gray and green surfaces of figure 3), a no-slip boundary condition is applied for $\mathbf{u}$ with a homogeneous Neumann condition for all the scalars ρ, Y_1 and P. At the outlet boundaries (red surfaces of figure 3), a fixed pressure $P = \rho_{am} g z$ is imposed for a considered height z with a homogeneous Neumann condition for $\mathbf{u}$. A homogeneous Neumann condition is imposed on ρ and Y_1 if $\mathbf{u}.\hat{\eta} \geq 0$; $\hat{\eta}$ is the outward unit normal at the outlet surfaces. Otherwise, the Dirichlet conditions $\rho = \rho_{am}$ and $Y_1 = 0$ are imposed.

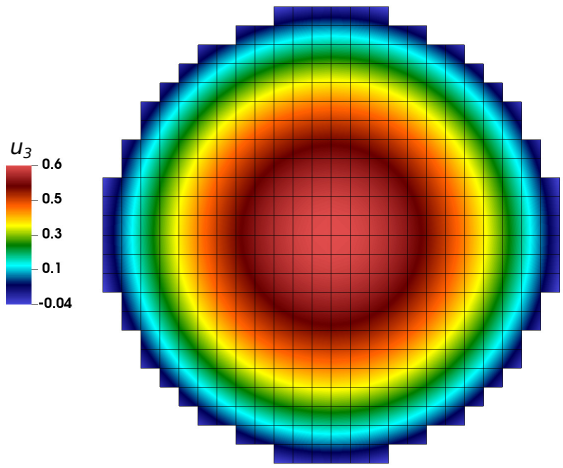

FIG. 6: Mesh 1: parabolic u_3 velocity profile prescribed at the inlet boundary condition.

D. Simulations management and statistical recordings

- Mesh 1:

For the first calculation performed with Mesh 1, the whole cavity is filled at the initial state with pure air at rest ($Y_1 = 0$ and $\mathbf{u} = 0$). The physical time of the simulation (till present) is about 175 seconds. Two monitoring points are considered to control the simulation. The first is located near the left wall at the spatial position $S_1 = (0, 0.44, 0.95)$ [m] which corresponds to the highest minicatharometer placed in the experimental study. $S_2 = (0, 0.44, 0.9)$ [m] corresponds to the second probe which is placed in the middle of the top vent. Figure 7 (top) depicts the temporal evolution of the hydrogen volume fraction X_1 and of the vertical velocity component u_3 at the probe S_1, while that of X_1 and the horizontal velocity component u_1 at probe S_2 (bottom).

It can be clearly noted that the flow is non-laminar and that significant fluctuations take place. The simulation is still in progress and we are waiting for a longer time to achieve a better quasi-steady state behavior. In the present paper, the time required to attain a quasi-steady state solution is assumed to be at 120 seconds. Thus the statistical fields presented in the remaining part of the document have been recorded starting from $t_{\text{start}} = 120$ s with a frequency $f = 1/\delta t$ Hz; δt denotes the time step of the simulation. For Mesh 1, the minimum time step recorded is about $\delta t \approx 3 \times 10^{-4}$ s. The computational cost of the simulation is about 6 s/δt, where about 80% of this time is devoted to the resolution of the pressure-projection algorithm.

In the sequel, $< \cdot >_t$ will denote the time averaged quantity calculated for a considered field $\varphi(t)$ as

$$< \varphi(t) >_t = \frac{1}{t - t_{\text{start}}} \int_{t_{\text{start}}}^{t} \varphi(t) dt. \tag{9}$$

- Mesh 2:

The initial condition in the second calculation performed on Mesh 2 is not the same as that of the first case. In order to accelerate the transient solution, the field variables predicted with Mesh

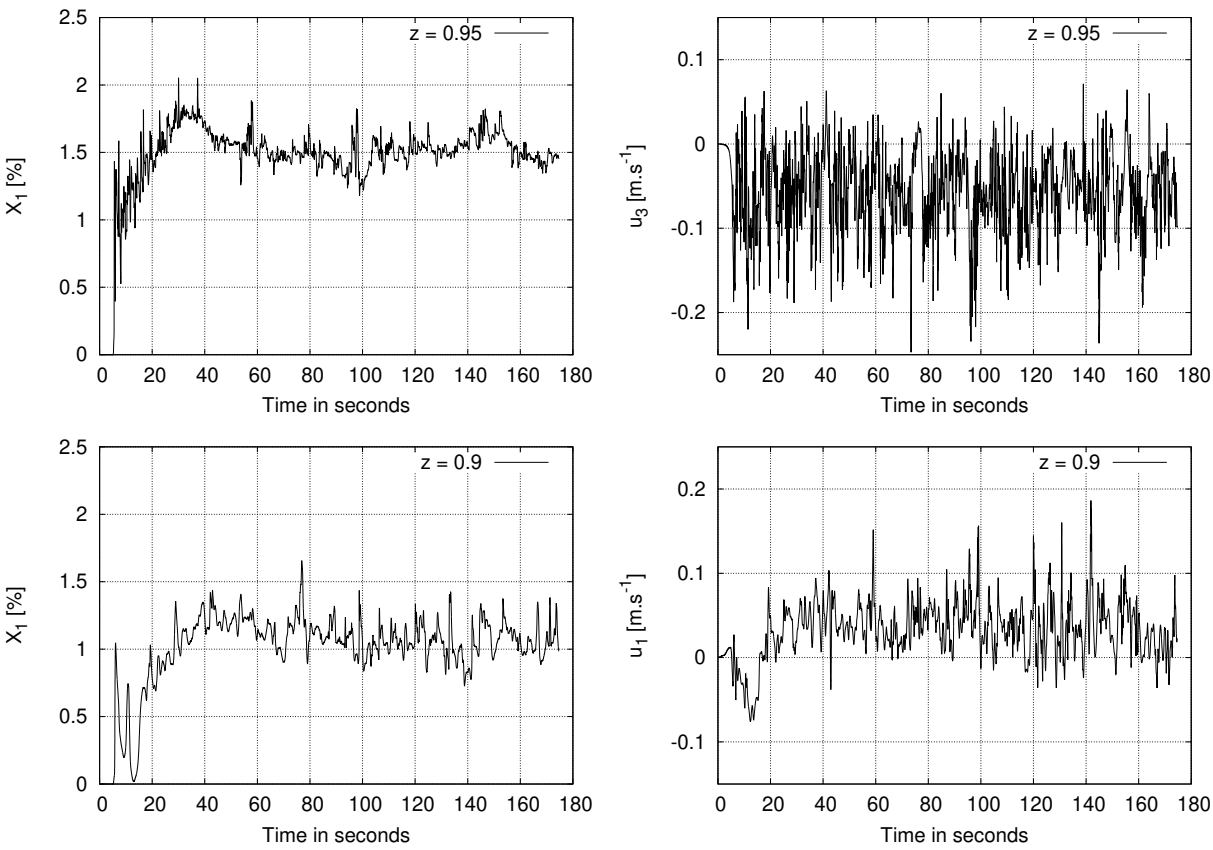

FIG. 7: Mesh 1: temporal evolution of X_1 and u_3 at probe S_1 (top), of X_1 and u_1 at probe S_2 (bottom).

1 at $t = 140$ s are interpolated onto Mesh 2; mainly the instantaneous $\mathbf{u}$ and Y_1 fields. In our case, and since the simulation is carried out on 50047 MPI procs, the highly performant library MEDCoupling is employed with its parallel interpolator "InterpKernelDEC" in order to achieve an efficient and precise parallel interpolation [19]. Figure 8 depicts the interpolated density ρ iso-contours in the mid-vertical xz-plane ($y = 0$) and thus identifies the initial condition for the second calculation.

For Mesh 2, the minimum time step recorded is about $\delta t \approx 1 \times 10^{-4}$ s with a computational cost about 10 s/δt. The calculation is currently in progress and only 5 physical time seconds are currently simulated. For this reason, only instantaneous results are provided in the present paper for the DNS performed on Mesh 2.

IV. RESULTS

This section describes the flow pattern recorded in the simulated configuration. Instantaneous fields obtained with Mesh 1 and Mesh 2 are presented first. Time-averaged fields are afterwards used to illustrate the mean flow distribution (only presented for Mesh 1 since the second calculation is still in its transient zone). Comparisons versus experimental data are finally considered.

FIG. 8: Mesh 2: density ρ iso-contours in the mid-vertical xz-plane ($y = 0$) at the initial state.

A. Instantaneous flow pattern

The flow pattern in the mid-vertical xz-plane ($y = 0$) at $t = 145$ s is depicted by the velocity magnitude $|\mathbf{u}| = (u_1^2 + u_2^2 + u_3^2)^{1/2}$ iso-contours in figure 9. Similarly, the instantaneous vorticity magnitude $|\boldsymbol{\omega}|$ iso-contours are considered in figure 10 for the same physical time and in the same plane. Both figures illustrate the entrainment of fresh air from the bottom vent resulting from the hydrogen injection. It can be noted in both calculations that the heavy air inflow impacts the rising light buoyant jet in a vertical section almost equivalent to the vent's height (Mesh 1 at the left and Mesh 2 at the right). As a consequence of the air/hydrogen impact, the buoyant jet axis deviates towards the facing wall. This cross-flow behavior has been well reported and documented in [7, 9] with a similar configuration. However, and since the volume of the cavity in this study is much bigger than that considered in their work, the buoyant jet remains far from the lateral solid boundaries of the enclosure.

Due to the continuous injection of hydrogen, the buoyant jet impacts the top ceiling. The flow afterwards separates in two directions, to the left where a recirculation zone builds near the top left corner, and to the right where the mixture leaves the cavity due to the buoyancy aspiration from the top vent. Qualitatively speaking, no effect of a flow-blockage is recorded since the fluid exiting from the higher vent is freely evacuated by buoyancy from the top of the exterior region. This explains the efficiency and the enhanced passive ventilation system of the considered fuel cell configuration.

Regarding the influence of the Mesh on the numerical resolution, it can be qualitatively noted from figures 9 and 10 that Mesh 2 captures better the small turbulent structure of the flow. In particular, the entrainement at the buoyant-jet border is better reproduced in the vicinity of the release position with Mesh 2. To illustrate, a zoomed region in the vicinity of the injection is considered in figure 11 where the $|\mathbf{u}|$ iso-contours are presented (same contour levels as figure 9).

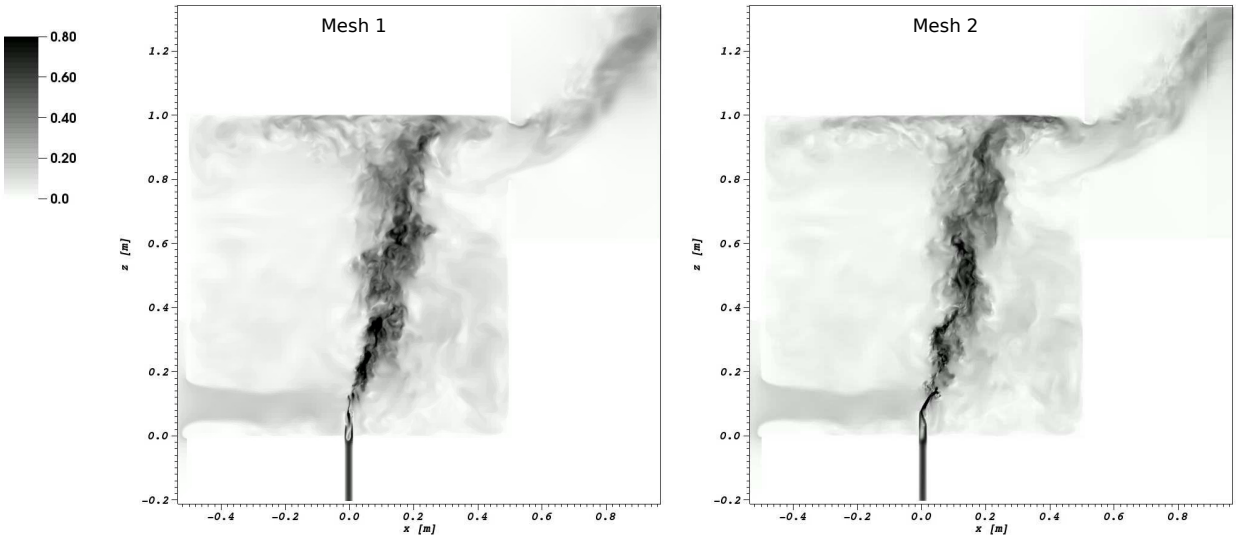

FIG. 9: Instantaneous velocity magnitude $|\mathbf{u}|$ iso-contours in the mid-vertical xz-plane ($y = 0$) at $t = 145$ s. Left: Mesh 1, right: Mesh 2.

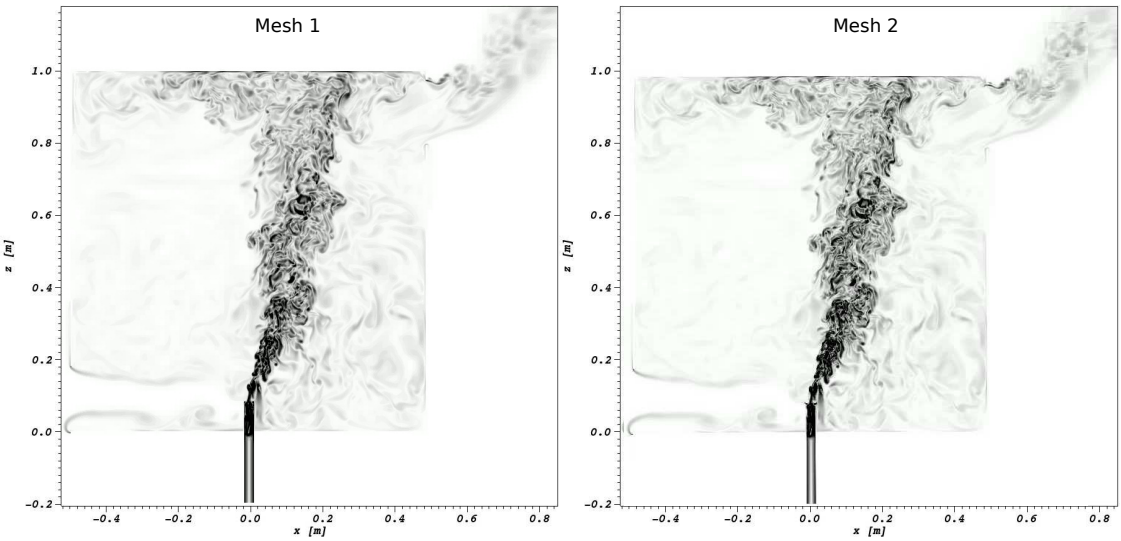

FIG. 10: Instantaneous vorticity magnitude $|\boldsymbol{\omega}|$ iso-contours in the mid-vertical xz-plane ($y = 0$). Left: Mesh 1 at $t = 175$ s, right: Mesh 2 at $t = 145$ s.

It is clear how the small vortices that entrain ambient air with rising hydrogen are much better resolved in the second calculation. This is not surprising and is expected since the grid size of Mesh 2 is smaller than the estimated Kolmogorov length scale and thus all turbulent length scales should be captured.

In the upper part of the cavity, mainly in the plume zone for $z \gtrsim 0.4$ m, the influence of the mesh is not that important where Mesh 1 is sufficient to capture all the scales. This result is also expected and is coherent with the estimated Kolmogorov length scale (figure 4). Moreover, as stated in [20, 21], the most challenging part of this problem is to capture correctly the jet-to-plume transition that is located few diameters above the injection. In this zone, the smallest length scales

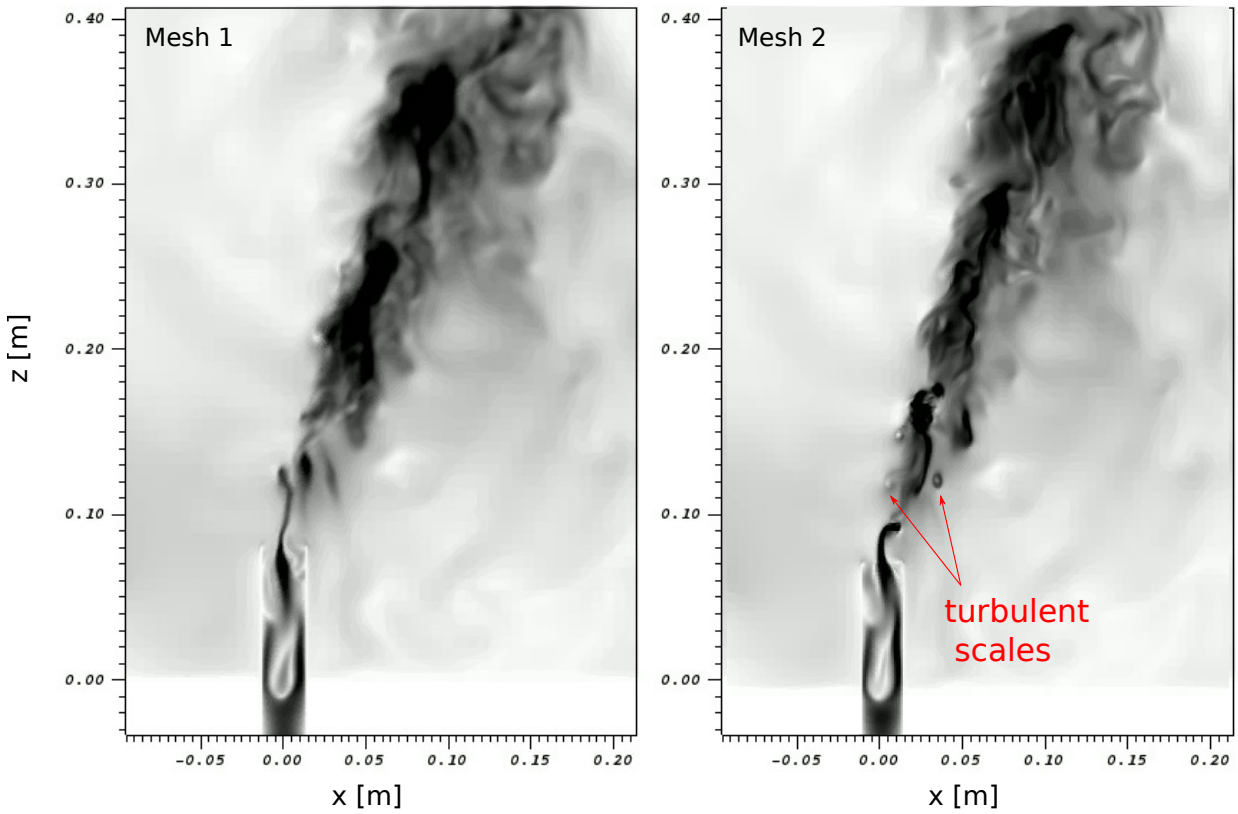

FIG. 11: $|\mathbf{u}|$ iso-contours in the vicinity of the release position illustrating the small turbulent scales reproduced by Mesh 2 (right).

take place due to the Rayleigh-Taylor instabilities which build due to the presence of a heavy fluid (air) above a light one (hydrogen). This confirms again why the influence is only observed in the lower part of the cavity where Mesh 2 is required to capture correctly the transition.

B. Time-averaged flow pattern

Figure 12 illustrates the time-averaged flow pattern in the mid-vertical xz-plane ($y = 0$) where the iso-contours of $< |\mathbf{u}| >_t$ are sketched. It can be clearly noted that the sharp cross-flow leads to an inclination of the buoyant-jet axis all along the height H. As stated previously, it can be noted that the cross-flow zone is situated at the bottom in a vertical section almost equivalent to the vent's height. Moreover, the mean distribution clearly reflects the effect of the natural ventilation in the system where the mixture evacuates freely at the top surface of the upper exterior region.

The time-averaged velocity magnitude $< |\mathbf{u}| >_t$ is described quantitatively in figure 13 by its vertical profile along the inclined axis of the buoyant jet. Starting from inner release position situated at $z = 0.08$ m, the jet accelerates due to the gravitational forces to take a maximum value of about 0.78 m.s^{-1} at $z = 0.1$ m. Above this height, the velocity magnitude reduces gradually all along the height of the cavity. As detailed thoroughly in the work of [9], the sharp decrease of the velocity profile between $0.1 \lesssim z \lesssim 0.2$ m corresponds to the jet-to-plume transitional zone. Such

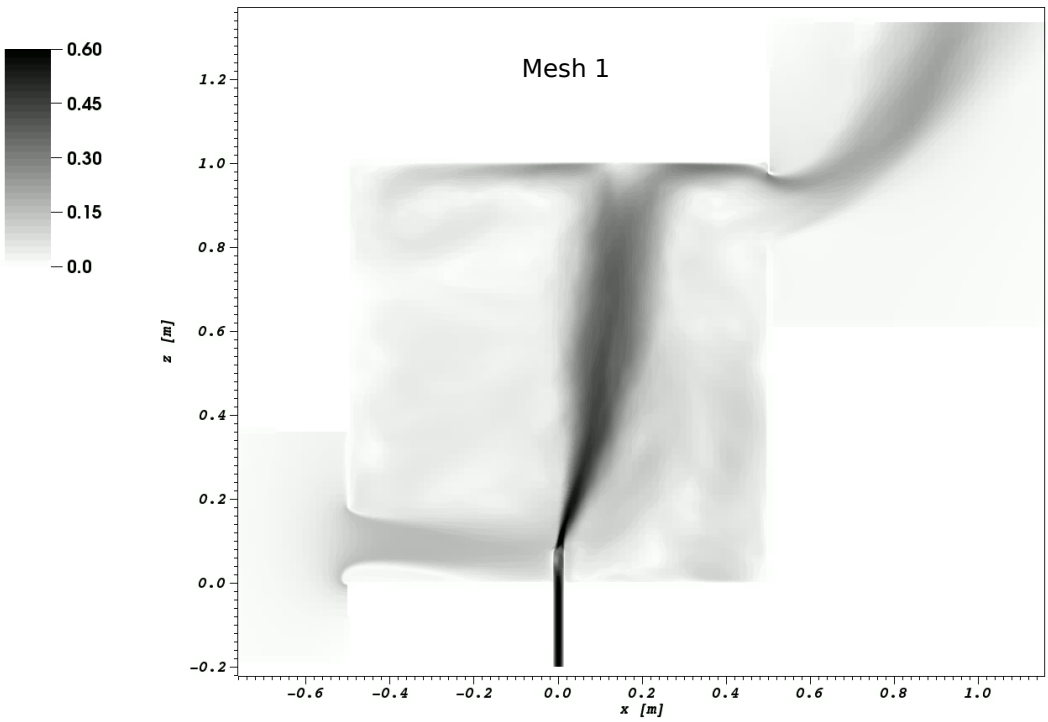

FIG. 12: Mesh 1: $< |\mathbf{u}| >_t$ iso-contours in the mid-vertical xz-plane ($y = 0$).

behavior is expected in varying density buoyant jet flows.

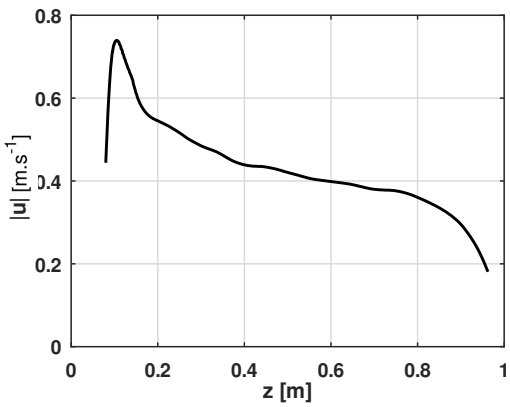

FIG. 13: Mesh 1: $< |\mathbf{u}| >_t$ vertical distribution along the inclined axis of the buoyant jet.

To illustrate the cross-flow effect and its influence on the time-averaged flow pattern, $< |\mathbf{u}| >_t$ iso-contours are depicted in a horizontal xy-plane situated at $z = 0.1$ m (figure 14, left). It can be clearly noted that the air-inflow passing the lower vent creates an almost uniform distribution in the left part of the cavity and pushes the jet to the right (black zone in the middle of the plane). Calm regions behind the jet axis (white iso-contours) explain how the flow separates while impacting the jet. This is a well known phenomenon in numerical simulations of jet flows subjected to a cross-flow [9]. The separated inflow continues afterward in its horizontal direction to impact the solid boundary and creates two counter-rotating vortices as shown in the same figure at the right corners.

Another influence of the cross-flow is noted on the internal structure of the jet. Figure 14 (right) depicts the iso-contours in a zoomed region around the jet axis situated in the same horizontal plane. The vector field is sketched on the same figure to illustrate the flow separation described previously. It can be clearly noted that the jet looses its circular structure and takes a *horseshoe-like* shape due to the circular flow that takes place at its border. This is also a well know behavior detailed and reported previously in the work of [7, 9]. However, it can be clearly noted that the statistical fields are not converged yet as the flow is expected to be perfectly symmetrical. Further statistical recordings and still in progress where a detailed convergence analysis will be considered later.

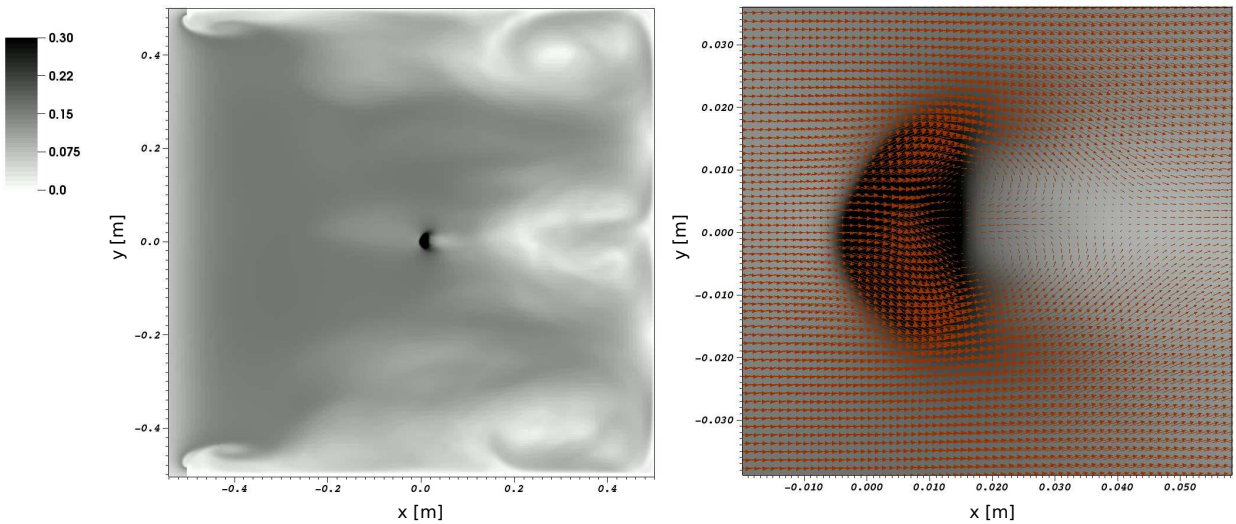

FIG. 14: Mesh 1: $< |\mathbf{u}| >_t$ time-averaged flow pattern in the horizontal xy-plane ($z = 0.1$ m). Left: iso-contours, right: iso-contours superposed by the vector field in a zoomed region.

Finally, the time-averaged velocity component normal to the vent surfaces is considered to describe the in/out flows at the top and bottom vents. The $< u_1 >_t$ iso-contours are depicted for both vents in figure 15. Solid black contour denotes a zero velocity level separating the negative and positive $< u_1 >_t$ values.

The iso-contours show that almost uniform inflow takes place at the bottom vent (figure 15, bottom). At the lower surface of this vent, and at its extremities, an outflow layer develops with much reduced velocity values (in absolute value). This is most probably related to the fact that the vents are not placed at the same wall. More precisely, the lower vent air inflow can lead to a global rotational flow in the lower part of the cavity which leaves afterwards from the lower part of the vent. This point will be investigated in a future study.

Unlike the behavior recorded at the bottom vent, the iso-contours of the time-averaged horizontal velocity component show a non-uniform distribution at the top vent (figure 15, top). A pure outflow takes place almost along the entire vent surface, except in a small layer situated in its lower surface (see the black contour line). The maximal values are situated in the middle at a top-thin layer where an exiting jet develops to evacuate the mixture. At the extremities of the vent, the flow exits in a rounded shape due to the counter-rotating flow that builds at the top of the cavity due to the impact with the ceiling. Again, it can be clearly noted that the distribution is not symmetrical and that the convergence of the statistical fields should be verified.

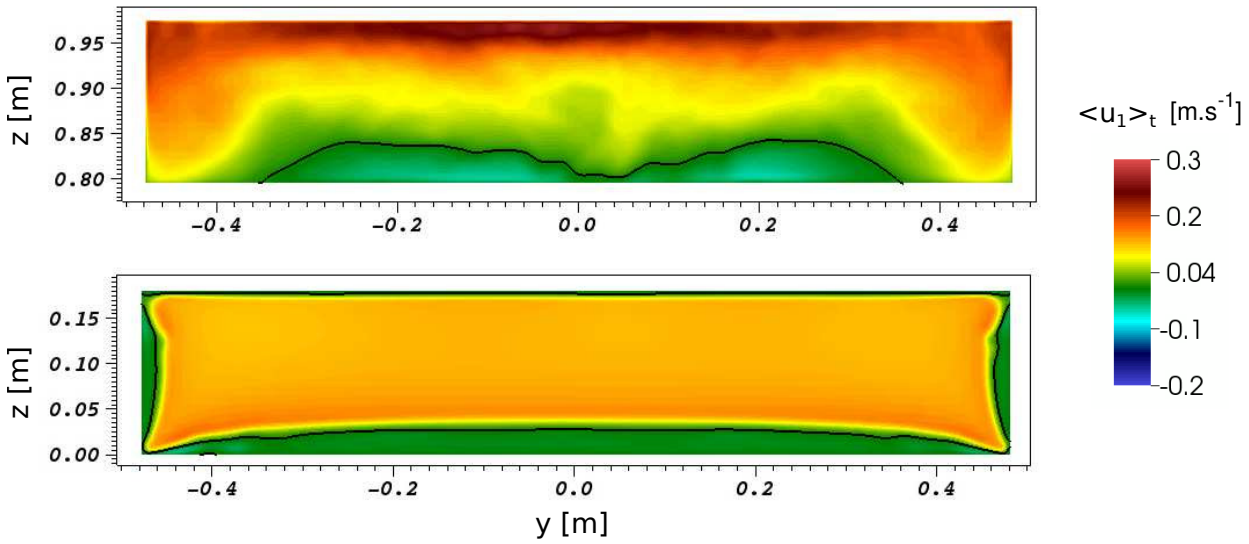

FIG. 15: Mesh 1: $< u_1 >_t$ iso-contours at the top-vent (top) and bottom-vent (bottom) surfaces.

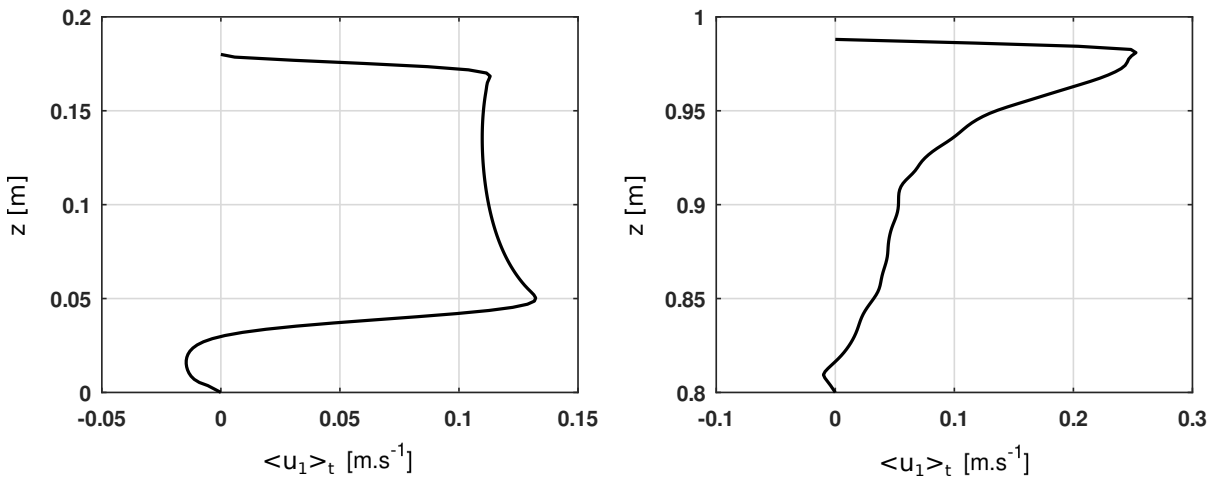

FIG. 16: Mesh 1: $< u_1 >_t$ vertical profiles at the middle of the bottom-vent (left) and top-vent (right) surfaces.

For a quantitative description, $< u_1 >_t$ vertical profiles are considered in figure 16 at the middle of both vents surfaces. At the lower vent, the vertical profile shows that the inflow is much more important than the outflow which takes place in about a $z \approx 2$ cm (figure 16, left). Moreover, an inverted parabola-like inflow distribution is recorded, similarly to what had been described previously by [7, 9]. This explains again the necessity of modeling an exterior region in the computational domain to approach the natural in/out-flow conditions.

At the top vent (figure 16, right), the vertical profile shows that the inflow is almost negligible, compared to the outflow, and takes place along about 1 cm (at the bottom surface). Above this height ($z \approx 0.81$ m), $< u_1 >_t$ values increase almost linearly till $z \approx 0.93$ m. Afterwards, a sharp increase takes place due to the presence of the exiting jet at the top layer where a maximum is recorded with $< u_1 >_t = 0.25$ m.s^{-1}. Again, a convergence analysis is required to quantify the

quality of the statistical fields that seem to be not converged yet.

C. Comparisons versus experimental measurements

In this subsection, the hydrogen time-averaged volume fraction is analyzed. Figure 17 depicts the $< X_1 >_t$ iso-contours in the mid-vertical xz-plane at $y = 0$ (left) and in the vertical yz-plane at $x = 2$ cm (right). As discussed previously, the efficient passive ventilation of the simulated configuration leads the exiting flow to evacuate freely from the enclosure without any blockage phenomenon. Thus, as noted qualitatively from both figures, a homogeneous mixture develops at the upper part of the cavity without any stratification. It can be stated that the counter-rotating vortices which develop at the top of the cavity play an important role in diluting this homogeneous mixture (see figure 18). Recall that this distribution is expected in ventilated configurations as the theory of Linden et al. states [22].

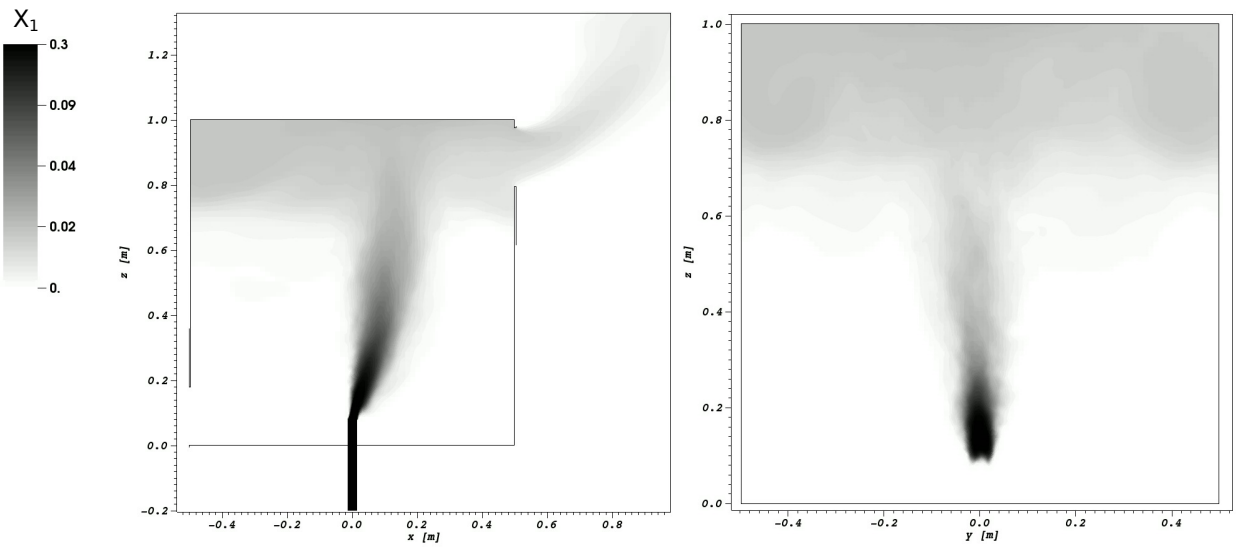

FIG. 17: Mesh 1: $< X_1 >_t$ iso-contours in the mid-vertical xz-plane at $y = 0$ (left) and in the vertical yz-plane at $x = 2$ cm (right).

For a quantitative description, a vertical $< X_1 >_t$ profile is plotted in figure 19 in the same position as the 15 minicatharometers used in the experimental study. The measured $< X_1 >_t$ values are described by symbols on the graph, while the black solid line corresponds to the DNS.

It can be clearly noted that the agreement between the DNS and the experimental measurements is very good. In particular, the numerical simulation agrees with the experiment in three main points: the presence of a bi-layer distribution with a top homogeneous layer at first, the height of the interface separating both layers at second, the maximal hydrogen concentration in the homogeneous layer at last. For a quantitative comparison, both the DNS and the experiment record about 1.6% of hydrogen in the upper homogeneous layer; the absolute difference is about 0.1% which can be originating either from the experiment (measurement error) or from the DNS (discretization error).

This result is extremely important and breaks the limitations shown previously with statistical

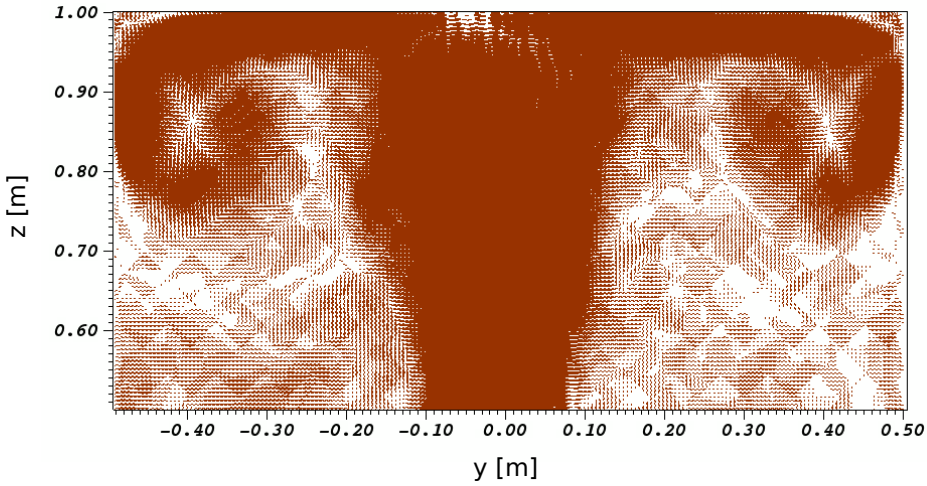

FIG. 18: Mesh 1: time-averaged velocity field at the top of the cavity in the vertical yz-plane at $x = 2$ cm.

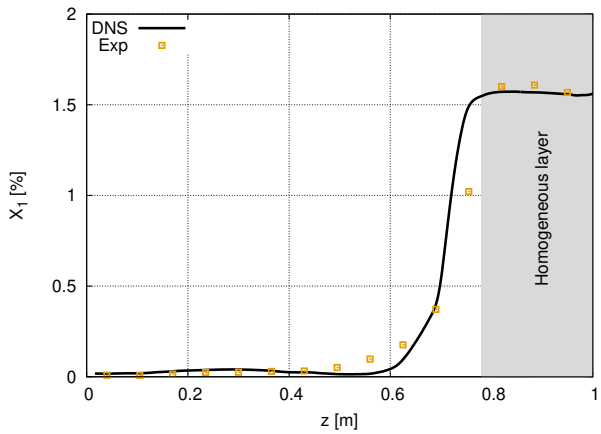

FIG. 19: Mesh 1: $< X_1 >_t$ vertical profile near the wall along the 15 minicatharometers used in the experimental study. DNS: solid black line, experiment: symbols.

RANS approaches and LES models that were not able to reproduce correctly a Linden configuration for this particular release condition [5, 6]. We emphasize that the discrepancy between the DNS and the measured concentration at $z = 0.755$ m is related to interface position which is slightly lower in the DNS. This is probably related to the fact that the statistical data are not yet converged. Further investigations will be carried out later when both the time averaged and the RMS recordings converge.

V. CONCLUDING REMARKS

In this paper, numerical results have been presented from two direct numerical simulations (DNS) for a light buoyant hydrogen jet developing in a two-vents cavity. The study mimics one of the experimental investigations carried out on the 1 m^3 DRHyS facility with a leak flow rate of 10.4

Nl.min^{-1}. Two sufficiently large exterior regions have been added to the computational domain to model correctly the exchange between the in/out flows at both vents and the outer environment. The high performance computing (HPC) platform TRUST is employed where the computational domain is distributed up to 5.10^4 central processing unit (CPU) cores.

Preliminary results have been presented in this paper as far as the numerical simulations are still in progress to achieve a convergent statistical fields. Two meshes have been used where Mesh 1 consists of about 250 million cells, while Mesh 2 of about two billion cells and is verified to be at the level of both the Kolmogorov and Batchelor length scales. Instantaneous data have been presented for both calculations while time-averaged fields are only presented for the first as far as statistical recordings with Mesh 2 are still in progress.

It has been figured out that the fine mesh improves the resolution in the lower part of the cavity, in particular in the vicinity of the hydrogen release position. As detailed thoroughly in the paper, this region defines the jet-to-plume transition zone where sharp Rayleigh-Taylor instabilities take place. As a consequence, the smallest flow structures are situated in this zone and thus require a very fine resolution. On the contrary, numerical results show that Mesh 1 is sufficient to capture all scales in the upper part of the cavity.

A thorough description of the time-averaged flow structure is presented where the cross-flow effect is characterized. Both the expected deviation and deformation of the buoyant jet axis are well reproduced by the mean flow-pattern. A rare situation is noted for the horizontal velocity component at the lower vent surface where both in- and out-flow directions are observed simultaneously. The efficiency of the passive ventilation in the considered configuration is highlighted where no density stratification takes place.

Finally, the comparisons versus the experimental measurements show a very good agreement where both the bi-layer Linden regime and the maximal concentration in the top homogeneous layer are correctly reproduced by the DNS. This result is extremely important and breaks the limitations shown previously with statistical RANS approaches and LES models. Further investigations will be carried out later when both the time averaged and the RMS data converge due to further data accumulation.

Acknowledgments

This work was granted access to the HPC resources of TGCC IRENE-ROME under the allocations A0092A12033 made by GENCI.

[1] G. Bernard-Michel and D. Houssin-Agbomson, *Comparison of helium and hydrogen releases in 1 m3 and 2 m3 two vents enclosures: Concentration measurements at different flow rates and for two diameters of injection nozzle*, International Journal of Hydrogen Energy **42**, 7542 (2017), ISSN 0360-3199.

[2] B. Cariteau and I. Tkatschenko, *Experimental study of the concentration build-up regimes in an enclosure without ventilation*, international journal of hydrogen energy **37**, 17400 (2012).

[3] B. Cariteau and I. Tkatschenko, *Experimental study of the effects of vent geometry on the dispersion of a buoyant gas in a small enclosure*, International Journal of Hydrogen Energy **38**, 8030 (2013), ISSN 0360-3199.

[4] B. Fuster, D. Houssin-Agbomson, S. Jallais, E. Vyazmina, G. Dang-Nhu, G. Bernard-Michel, M. Kuznetsov, V. Molkov, B. Chernyavskiy, V. Shentsov, et al., *Guidelines and recommendations for indoor use of fuel cells and hydrogen systems*, International Journal of Hydrogen Energy **42**, 7600 (2017), ISSN 0360-3199, special issue on The 6th International Conference on Hydrogen Safety (ICHS 2015), 19-21 October 2015, Yokohama, Japan.

[5] G. Bernard-Michel, B. Cariteau, J. Ni, S. Jallais, E. Vyazmina, D. Melideo, D. Baraldi, and A. Venetsanos, in *Proceedings of ICHS 2013* (2013).

[6] S. Giannissi, V. Shentsov, D. Melideo, B. Cariteau, D. Baraldi, A. Venetsanos, and V. Molkov, *Cfd benchmark on hydrogen release and dispersion in confined, naturally ventilated space with one vent*, International Journal of Hydrogen Energy **40**, 2415 (2015), ISSN 0360-3199.

[7] E. Saikali, G. Bernard-Michel, A. Sergent, C. Tenaud, and R. Salem, *Highly resolved large eddy simulations of a binary mixture flow in a cavity with two vents: Influence of the computational domain*, International Journal of Hydrogen Energy **44**, 8856 (2019), ISSN 0360-3199.

[8] G. Bernard-Michel, E. Saikali, A. Sergent, and C. Tenaud, *Comparisons of experimental measurements and large eddy simulations for a helium release in a two vents enclosure*, International Journal of Hydrogen Energy **44**, 8935 (2019), ISSN 0360-3199.

[9] E. Saikali, A. Sergent, Y. Wang, P. L. Quere, G. Bernard-Michel, and C. Tenaud, *A well-resolved numerical study of a turbulent buoyant helium jet in a highly-confined two-vented enclosure*, International Journal of Heat and Mass Transfer **163**, 120470 (2020), ISSN 0017-9310.

[10] F. A. Williams, *Combustion theory* (CRC Press, 2018).

[11] S. Hamimid, M. Guellal, and M. Bouafia, *Numerical study of natural convection in a square cavity under non-boussinesq conditions*, Thermal Science pp. 84–84 (2014).

[12] B. Müller and B. Muller, *Low mach number asymptotics of the navier-stokes equations and numerical implications* (1999).

[13] C. Wilke, *A viscosity equation for gas mixtures*, The journal of chemical physics **18**, 517 (1950).

[14] CEA, *TRUST code version 1.8.2*, `https://sourceforge.net/projects/trust-platform/`.

[15] Y. Saad, *Iterative methods for sparse linear systems* (SIAM, 2003).

[16] PETSc, *Portable, extensible toolkit for scientific computation (petsc) library*, `https://www.mcs.anl.gov/petsc/`.

[17] S. Chhabra, P. Huq, and A. K. Prasad, *Characteristics of small vortices in a turbulent axisymmetric jet*, Journal of fluids engineering **128**, 439 (2006).

[18] G. K. Batchelor, *Small-scale variation of convected quantities like temperature in turbulent fluid part 1. general discussion and the case of small conductivity*, Journal of Fluid Mechanics **5**, 113 (1959).

[19] platform V9.6.0 SALOME, *https://www.salome-platform.org/news*.

[20] W. Rodi, *Turbulent buoyant jets and plumes*, vol. 3 (Pergamon press Oxford, 1982).

[21] E. Saikali, Ph.D. thesis, *Numerical modelling of an air-helium buoyant jet in a two vented enclosure*, Sorbonne Université (2018).

[22] P. Linden, G. Lane-Serff, and D. Smeed, *Emptying filling boxes: the fluid mechanics of natural ventilation*, Journal of Fluid Mechanics **212**, 309 (1990).